PAPER

Check for updates

Homochiral Dy₂Zn₂ zero-field single-molecule magnets derived from (R)/(S)-2-methoxy-2-phenylacetic acids

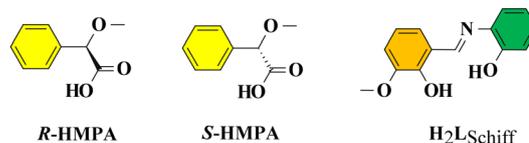Cai-Ming Liu, [ID] *[a] Xiang Hao[a] and Yi-Quan Zhang [ID] *[b]

Despite the unique advantages of multifunctional integration at the nanoscale, chiral zero-field single-molecule magnets (SMMs), especially those based on homochiral carboxylic acids, are still difficult to obtain. Herein, homochiral (R)/(S)-2-methoxy-2-phenylacetic acids (R-HMPA)/(S-HMPA) were selected as the bridging ligands to assemble a pair of Dy₂Zn₂ enantiomers based on the Schiff base ligand (E)-2-((2-hydroxy-3-methoxybenzylidene)amino)phenol (H₂L_Schiff), [Dy₂Zn₂(S-MPA)₂(L_Schiff)₄(DMF)₂]·2DMF (S-**1**) (DMF = N,N-dimethylformamide) and [Dy₂Zn₂(R-MPA)₂(L_Schiff)₄(DMF)₂]·2DMF (R-**1**), which possess a [Dy₂Zn₂O₆] defective dicubane core. The CD spectra of R-**1** and S-**1** confirmed their enantiomeric nature and chiral optical activities. Magnetic studies revealed that they are good zero-field SMMs, with a relatively large U_{eff}/k value of 234.6 K at 0 Oe and an obvious hysteresis loop at 3.0 K; notably, these magnetic properties could be explained using *ab initio* calculations.

Introduction

Recently, chiral single-molecule magnets (SMMs) have attracted increasing attention, mainly because chirality offers some additional physical properties, such as ferroelectricity,[1–4] second-order nonlinear optical properties,[5–9] magnetochiral dichroism (MChD),[10,11] and circularly polarized luminescence (CPL).[12–15] As nanoscale molecules with magnetic bistability, SMMs have potential applications in high-density information storage, quantum computing and other fields.[16–18] After the introduction of other properties through chirality, chiral SMMs have further become a special class of nanoscale multifunctional molecular materials. For example, with the addition of ferroelectric properties, they become multiferroic molecular materials, which can respond to electric and magnetic field signals at the same time, increasing the dimension of high-density information storage.[1–4] Likewise, with the addition of MChD, chiral SMMs can realize the optical readout of magnetically stored signals.[10,11] Obviously, these kinds of multidimensional, signal-responsive, nanoscale, and multifunctional molecular materials can meet the requirements of the contemporary high-tech fields of intelligence, integration, and

micro-nano miniaturization. However, the trend of racemization in solution makes the synthesis of homochiral SMMs a great challenge.[19]

Although chiral SMMs can be assembled using achiral ligands by means of spontaneous resolution of chirality through coordination assembly, this is applicable only to a minority.[20–22] In fact, most chiral SMMs are assembled directly from chiral ligands.[23–38] When Schiff bases and reduced Schiff bases,[23–29] β-diketonates,[30–32] phosphoric acids,[33] phosphates,[34] axial ligands,[35–38] and helical ligands[10] are endowed with chirality, they can be used to construct chiral SMMs, especially chiral SMMs with Ln(III) ions, which include 4f SMMs and 3d–4f SMMs. Unfortunately, homochiral carboxylic acids,[39–42] which are common and relatively inexpensive ligands, do not play a major role in the construction of chiral SMMs, especially zero-field homochiral SMMs. Herein, we report a pair of Dy₂Zn₂ enantiomers based on (R)/(S)-2-methoxy-2-phenylacetic acids (R-HMPA/S-HMPA, Scheme 1) and a Schiff base formed by the condensation of o-vanillin and 2-aminophenol {H₂L_Schiff = (E)-2-((2-hydroxy-3-methoxybenzylidene)amino)phenol, Scheme 1}, [Dy₂Zn₂(S-

[a] Beijing National Laboratory for Molecular Sciences, CAS Key Laboratory for Organic Solids, Institute of Chemistry, Chinese Academy of Sciences, Beijing 100190, China.
E-mail: cmliu@iccas.ac.cn
[b] Ministry of Education Key Laboratory of NSLSCS, School of Physical Science and Technology, Nanjing Normal University, Nanjing 210023, China.
E-mail: zhangyiquan@njnu.edu.cn

Scheme 1 Structures of R-HMPA, S-HMPA and H₂L_Schiff.

MPA)$_2$(L$_{Schiff}$)$_4$(DMF)$_2$]·2DMF (S-**1**) (DMF = N,N-dimethylformamide) and [Dy$_2$Zn$_2$(R-MPA)$_2$(L$_{Schiff}$)$_4$(DMF)$_2$]·2DMF (R-**1**), which have a {Dy$_2$Zn$_2$O$_6$} defective dicubane core and show good zero-field SMM properties, with a large U_{eff}/k value of 234.6 K at 0 Oe and a clear hysteresis loop at 3.0 K.

Experimental

Materials and methods

All commercial chemicals and solvents were used directly without further purification. H$_2$L$_{Schiff}$ was synthesized using a method reported in the literature.[32]

Elemental analyses were performed on a Thermo Flash EA1112 elemental analyzer. Infrared spectra were recorded using a Bruker VERTEX 70v spectrophotometer with pressed KBr pellets. Powder X-ray diffraction (PXRD) spectra were obtained using a PANalytical Empyrean diffractometer with Cu–Kα radiation (λ = 1.5418 Å). Circular dichroism (CD) spectra were obtained using a Jasco J-1700 spectrometer. Magnetic properties were determined using a Quantum Design MPMS-XL5 (SQUID) magnetometer. The diamagnetism of all the constituent atoms was corrected using Pascal's constant.

Syntheses of Dy(R-MPA)$_3$ and Dy(S-MPA)$_3$

6.0 mmol R-HMPA or S-HMPA and 6.0 mmol LiOH·H$_2$O were added to 30 mL of water, an aqueous solution was obtained after stirring for 10 minutes, then 2.0 mmol DyCl$_3$·6H$_2$O was added to this solution and stirred for another 3 hours to obtain the precipitate of Dy(R-MPA)$_3$ and Dy(R-MPA)$_3$. The white precipitate was collected by filtration and dried in a vacuum. Yield: 80%.

Synthesis of R-1 and S-1

0.25 mmol H$_2$L$_{Schiff}$, 0.125 mmol Dy(R-MPA)$_3$ or Dy(S-MPA)$_3$, and 0.50 mmol Et$_3$N in 3 mL of DMF and 20 mL of MeOH were stirred for one hour, then 0.125 mmol Zn(CF$_3$SO$_3$)$_2$ was added and stirred for two hours. A yellow precipitate appeared, which was dissolved by adding 20 mL of CH$_2$Cl$_2$. The mixture was then stirred for half an hour and the obtained yellow solution was transferred to a beaker (50 mL), from which yellow single crystals of R-**1** or S-**1** could be grown by slowly volatilizing the solvent. Yield: 50–60% based on Dy.

Elemental analysis calcd (%) for C$_{86}$H$_{90}$Dy$_2$N$_8$O$_{22}$Zn$_2$ (R-1). C, 50.55; H, 4.44; N, 5.48; found: C, 50.46; H, 4.48; N, 5.43. IR (KBr, cm^{-1}): 3438(br w), 3054(w), 3024(w), 2982(w), 2931(w), 2825(w), 1669(s), 1589(s), 1545(w), 1479(m), 1457(s), 1387(m), 1338(w), 1299(w), 1285(w), 1251(w), 1225(s), 1179(w), 1103(w), 1085(w), 1041(w), 971(w), 928(w), 868(w), 817(w), 780(w), 735(s), 704(w), 683(w), 636(w), 614(w), 542(w), 508(w), 430(w).

Elemental analysis calcd(%) for C$_{86}$H$_{90}$Dy$_2$N$_8$O$_{22}$Zn$_2$ (S-1). C, 50.55; H, 4.44; N, 5.48; found: C, 50.49; H, 4.49; N, 5.45. IR (KBr, cm^{-1}): 3443(br, w), 3051(w), 3006(w), 2973(w), 2928(w), 2894(w), 2837(w), 2812(w), 1667(s), 1588(s), 1546(w), 1461(s), 1408(w), 1382(m), 1336(w), 1309(w), 1284(w), 1249(w), 1225 (s), 1179(w), 1102(w), 1075(w), 1001(w), 971(w), 926(w), 866(w),

816(w), 783(w), 731(s), 701(w), 676(w), 634(w), 579(w), 540(w), 509(w), 430(w).

Crystallography

Single-crystal X-ray diffraction analysis of R-**1** and S-**1** was performed using a Rigaku Synergy-R diffractometer with Cu–Kα radiation (λ = 1.54184 Å) at low temperatures. The Olex2.solve structure solution program was utilized to solve these two structures, which were refined using the ShelXL-2018 refinement package. All non-hydrogen atoms were refined anisotropically, and all hydrogen atoms were allowed for as riding atoms. The crystal data and structural refinement parameters of R-**1** and S-**2** are listed in Table 1.

Results and discussion

Syntheses and circular dichroism (CD) spectra

The multidentate ligand (E)-2-((2-hydroxy-3-methoxybenzylidene)amino)phenol(H$_2$L$_{Schiff}$) and its analogues have been used to assemble several Dy$_2$Zn$_2$ SMMs,[43–45] but chirality has never been involved. We expected that this Schiff base ligand could be utilized to synthesize the homochiral Dy$_2$Zn$_2$ SMMs along with homochiral carboxylic acids through a 'mixed ligand' assembly strategy. (R)/(S)-2-methoxy-2-phenylacetic acids (R/S-HMPA) were chosen in this study, and their Dy(III) complex precursors Dy(R-MPA)$_3$ and Dy(S-MPA)$_3$ were pre-synthesized, which were then reacted with H$_2$L$_{Schiff}$, Et$_3$N and Zn(CF$_3$SO$_3$)$_2$ in a DMF–MeOH–CH$_2$Cl$_2$ mixed solvent to yield R-**1** and S-**1** reproducibly. The reaction was carried out at room temperature, which usually avoids the rapid racemization of

Table 1 Crystal data and structural refinement parameters for R-**1** and S-**2**

	R-**1**	S-**1**
Formula	C$_{86}$H$_{90}$Dy$_2$N$_8$O$_{22}$Zn$_2$	C$_{86}$H$_{90}$Dy$_2$N$_8$O$_{22}$Zn$_2$
F_W	2043.39	2043.39
Crystal system	Monoclinic	Triclinic
Space group	P2$_1$	P2$_1$
a [Å]	12.85337(11)	12.90010(11)
b [Å]	16.76827(12)	16.81720(12)
c [Å]	20.35111(16)	20.47270(16)
α [°]	90.00	90.00
β [°]	105.0236(8)	105.6000(8)
γ [°]	90.00	90.00
V [Å^3]	4236.32(6)	4277.81(6)
Z	2	2
$\rho_{calc.}$ [g·cm^{-3}]	1.602	1.586
μ [mm^{-1}]	10.568	10.465
T [K]	104	170
λ [Å]	1.54184	1.54184
Reflections collected	55 372	67 781
Unique reflections	16 986	17 009
Observed reflections	16 729	15 198
Parameters	1094	1092
GoF[$I \geq 2\sigma(I)$]	1.021	1.009
$R_1[I \geq 2\sigma(I)$]	0.0281	0.0353
$_wR_2[I \geq 2\sigma(I)$]	0.0751	0.0860
Flack value	−0.0007(11)	0.0055(19)
CCDC	2463750	2463751

chiral complexes.[19] Notably, if *R*/*S*-HMPA were used directly in the reaction, or if other bases (such as LiOH) were used instead of Et$_3$N, it was difficult to obtain *R*-**1** and *S*-**1**. The high purity of the two samples *R*-**1** and *S*-**1** was confirmed by their powder X-ray diffraction (PXRD) spectra, which showed peaks that coincided well with the diffraction peaks simulated from their crystal structures (Fig. S1 and S2).

The enantiomeric nature and chiral optical activities of *S*-**1**/ *R*-**1** were confirmed by their CD spectra, which were measured in DMF solution (0.1 g L^{-1}) at room temperature (Fig. 1a). Mirror symmetry was observed in the CD curves of *S*-**1** and *R*-**1** at 280–550 nm: for *S*-**1**, there are a weak positive Cotton peak at 295 nm, a strong positive Cotton peak at 442 nm and a negative Cotton peak at 376 nm, while *R*-**1** has three Cotton peaks in opposite directions at the corresponding position (Fig. 1a). Accordingly, the UV-visible spectra of *S*-**1** and *R*-**1** exhibited two absorbance peaks at 301 nm and 420 nm, and a shoulder peak at around 380 nm (Fig. 1b). Therefore, the CD peak at 295 nm was caused by the π–π* transition of the benzene groups in the L$_{Schiff}^{2-}$ ligand, while the Cotton peaks at 376 nm and 442 nm could be attributed to the π–π* and n–π* transitions of the C=N group in the L$_{Schiff}^{2-}$ ligand, respectively.

Crystal structures

Analysis of the crystal structures of the enantiomers *R*-**1** and *S*-**1** revealed that both belong to the *P*2$_1$ space group, and the near-zero Flack values of 0.0055(19) and −0.0007(11) corresponded to *S*-**1** and *R*-**1**, respectively (Table 1), indicating that their single-crystal structures exhibited enantiomeric purity. Only the crystal structure of *S*-**1** is reported in detail here, as enantiomers exhibit crystal structures with mirror symmetry. As shown in Fig. 2, the host molecular structure of *S*-**1** consists of two Dy^{3+} cations, two Zn^{2+} cations, four L$_{Schiff}^{2-}$ anions, two *S*-MPA$^-$ anions, and two DMF terminal ligands. In addition, *S*-**1** contains some DMF solvent molecules in its lattice.
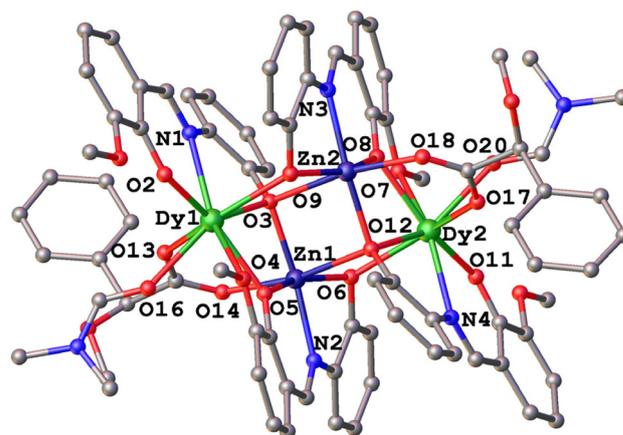

Fig. 2 Crystal structure of *S*-**1** (all the DMF solvent molecules and H atoms are omitted for clarity).

Two Dy^{3+} ions and two Zn^{2+} ions are interconnected by two triple-bridged phenoxo-O atoms and four double-bridged phenoxo-O atoms to form the [Dy$_2$Zn$_2$O$_6$] metal core, showing a defective dicubane topology, where the two defective cubanes share a common [Zn$_2$O$_2$] plane. Similar cases were observed in other Dy$_2$Zn$_2$ complexes that were based on the same Schiff base ligand.[44] This [Dy$_2$Zn$_2$O$_6$] metal core unit has a butterfly-shaped structure, where the [Zn$_2$O$_2$] plane forms the main part, while the two Dy^{3+} ions are located in the wing positions. The separation distances of Zn1···Zn2 and Dy1···Dy2 are 3.333 Å and 6.189 Å, respectively. Each Zn(II) ion has an octahedral geometry, which is coordinated by one N$_{imine}$ atom, one O$_{methoxy}$ atom and two O$_{phenoxide}$ atoms from one L$_{Schiff}^{2-}$ ligand, two O$_{phenoxide}$ atoms from two L$_{Schiff}^{2-}$ ligands, and one O$_{carbonyl}$ atom from one *S*-MPA$^-$ anion. Each Dy^{3+} ion has a [O$_7$N] coordination sphere, and is bonded by one N$_{imine}$ atom and two O$_{phenoxide}$ atoms from one L$_{Schiff}^{2-}$ ligand, one O$_{methoxy}$ atom and one O$_{phenoxide}$ atom from the second L$_{Schiff}^{2-}$ ligand, one O$_{phenoxide}$ atom from the third L$_{Schiff}^{2-}$ ligand, one O$_{carbonyl}$ atom from one *S*-MPA$^-$ anion, and one O atom supplied by one DMF terminal ligand. The coordination configurations of Dy1 and Dy2 were determined to be a biaugmented trigonal prism (C_{2v}) for Dy1 and a triangular dodecahedron (D_{2d}) for Dy2, as analysed with the SHAPE-2.1 software,[46] using the CShM values of 1.298 for C_{2v} and 1.447 for D_{2d} (Table S1). These configurations are obviously different from the seriously disordered Johnson elongated triangular bipyramid J14 geometry (D_{3h}) observed in [Zn$_2$Dy$_2$L$_4$(Ac)$_2$(DMF)$_2$]·4CH$_3$CN {H$_2$L = (*E*)-2-((2-hydroxy-3-methoxybenzylidene)amino)-4-methylphenol}.[45] Notably, the *S*-MPA$^-$ anion in *S*-**1** works as a bridging ligand, with two O$_{carbonyl}$ atoms being connected with one Zn^{2+} ion and one Dy^{3+} ion; in other words, its carboxyl group is a bridging ligand rather than a terminal ligand, similar to the carboxyl group on [Zn$_2$Dy$_2$L$_4$(Ac)$_2$(DMF)$_2$]·4CH$_3$CN.[45]

As an enantiomer, the crystal structure of *R*-**1** is mirror-symmetrical with that of *S*-**1** (Fig. 3). However, the Zn1···Zn2 separ-
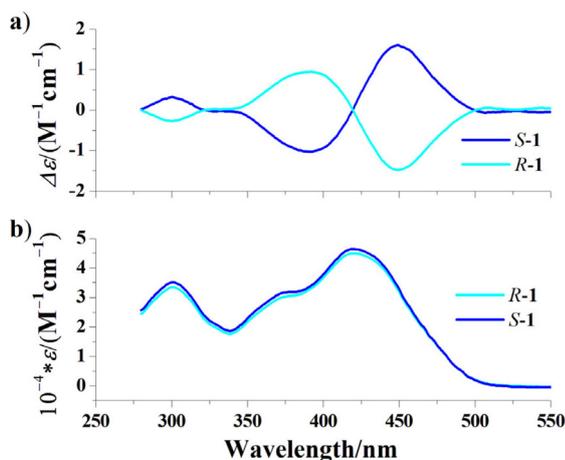

Fig. 1 CD spectra (5 mm optical path) (a) and UV spectra of *S*-**1**/*R*-**1** in DMF solution (*c* = 0.1 g L^{-1}) in the range of 280–550 nm at room temperature (b).
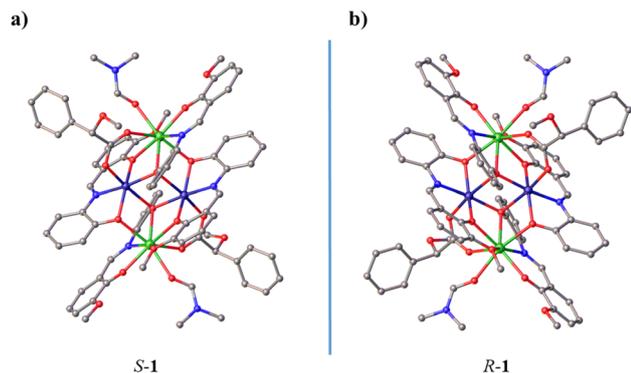
a)

S-**1**

b)

R-**1**

Fig. 3 Mirror symmetry of *S*-**1** (a) and *R*-**1** (b).

Fig. 5 χ'' *versus T* curves for *S*-**1** (H_{dc} = 0 Oe) (a); χ'' *versus ν* curves for *S*-**1** (H_{dc} = 0 Oe) (b); plot of $\ln(\tau)$ *versus* $1/T$ for *S*-**1** (H_{dc} = 0 Oe); the solid line represents the best fitting with QTM + Raman + Orbach (c); and hysteresis loop for *S*-**1** at 3.0 K with a normal sweep rate (100–300 Oe min^{-1}) (d).

ation distance in *R*-**1** is 3.327 Å, which is slightly shorter than that in *S*-**1** (3.333 Å), while the Dy1···Dy2 distance of 6.193 Å in *R*-**1** is slightly longer than that of *S*-**1** (6.189 Å).

Magnetic properties

Only the magnetic properties of the chiral isomer *S*-**1** were investigated, as enantiomers usually exhibit very similar magnetic properties. The room-temperature $\chi_M T$ value of *S*-**1** (28.33 cm^3 K mol^{-1}) is consistent with the theoretical value for the two isolated Dy^{3+} ions (28.34 cm^3 K mol^{-1}) (Fig. 4). The overall trend of the $\chi_M T$–*T* curve of *S*-**1** shows that $\chi_M T$ decreased slowly with a decrease in temperature due to the depopulation of the M_j levels of the Dy^{3+} ion. The curves of the magnetization of *S*-**1** as a function of the magnetic field at different low temperatures were then measured, and the corresponding *M*–*H*/*T* curves showed no coincidence at 2–6 K (Fig. S3), indicating magnetic anisotropy and/or the presence of low-lying excited states.

Meticulous measurements of the ac magnetic susceptibility of *S*-**1** revealed that it is a typical SMM. As shown in Fig. 5a, the χ''–*T* curves of *S*-**1** exhibited frequency-dependent peaks in the range of 50–1399 Hz at 0 Oe; meanwhile, its χ''-ν curves at
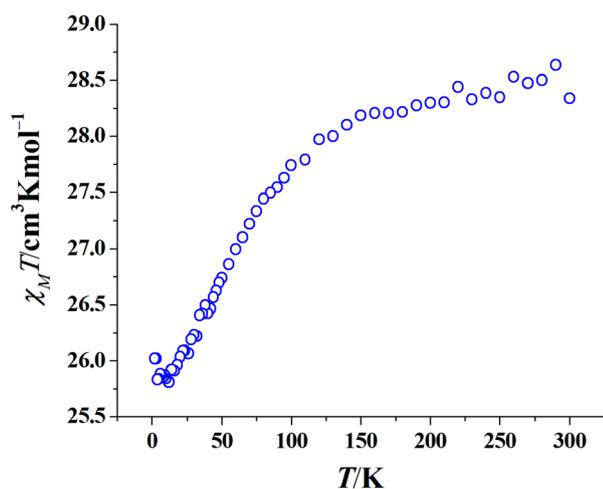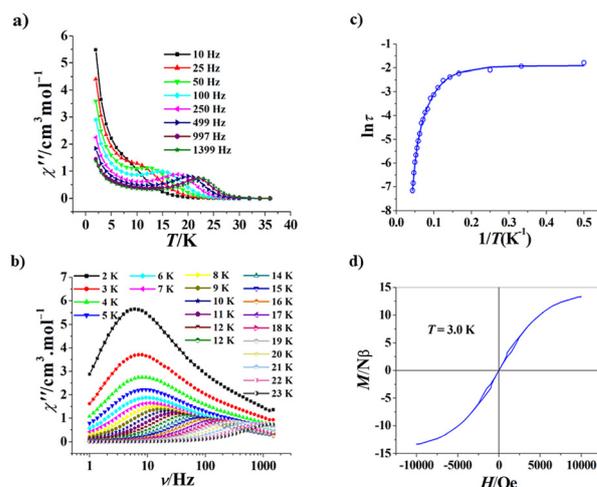
0 Oe also showed clear frequency dependence in the range of 2–23 K (Fig. 5b), from which the $\ln \tau$ *versus* $1/T$ plot was obtained (Fig. 5c); this plot deviated significantly from a straight line; thus, the formula $\tau^{-1} = \tau_{QTM}^{-1} + CT^n + \tau_0^{-1} \exp(-U_{eff}/kT)$, which accounts for QTM and the Raman and Orbach processes, was adopted to fit this curve, yielding τ_{QTM} = 0.148, n = 3.82, C = 0.0024 s^{-1} K$^{-3.82}$, U_{eff}/k = 234.6 K and τ_0 = 4.1 × 10^{-8} s. Both the n value (3.82) and the τ_0 value (4.1 × 10^{-8} s) of *S*-**1** are normal for SMMs.[17] The U_{eff}/k value (234.6 K) of *S*-**1** is large compared to that of most Dy$_2$Zn$_2$ SMMs with the same and similar L$_{Schiff}^{2-}$ ligands (≤166.0 K),[43,44] but smaller than that of [Zn$_2$Dy$_2$L$_4$(Ac)$_2$(DMF)$_2$]·4CH$_3$CN (305 K).[45] The relatively large energy barrier value of *S*-**1** is related to the diamagnetic Zn^{2+} ions, which can increase the charge density on the bridging oxygen atoms through polarization effects. Hence, the excited KDs were far away from the ground KDs, and the wavefunction overlap was minimized. Consequently, the energy barrier was increased by reducing the QTM probability.[47]

More importantly, a butterfly-shaped hysteresis loop was observed at 3.0 K for *S*-**1** (Fig. 5d), while most Zn$_2$Dy$_2$ SMMs with the same and similar L$_{Schiff}^{2-}$ ligands do not exhibit a hysteresis loop even at 1.9 K,[43,44] except for [Zn$_2$Dy$_2$L$_4$(Ac)$_2$(DMF)$_2$]·4CH$_3$CN, which has a hysteresis loop at 1.9 K.[45] Notably, *S*-**1** is a rare, chiral Dy–Zn zero-field SMM in that it displays a hysteresis loop at 3.0 K. The Cole–Cole curves at 2–21 K for *S*-**1** reveal some double magnetic relaxation features due to two kinds of coordination configurations for the Dy^{3+} ions, which could be fitted using the sum of two modified Debye functions (Fig. S4),[48–50] yielding the α_1 value of 0.001–0.181 and the α_2 value of 0.030–0.485.

We also investigated the effect of 1500 Oe, a commonly used dc magnetic field, on the magnetic relaxation properties

Fig. 4 Plot of $\chi_M T$ *versus T* for *S*-**1** (H_{dc} = 1000 Oe).

of S-**1**. The χ''–T curves of S-**1** at 1500 Oe showed more frequency-dependent peaks over a wider range of 1–1399 Hz (Fig. 6a). However, its χ''–ν curves at 1500 Oe indicated that its frequency-dependent peak range became narrower (8–23 K) (Fig. 6b), from which the ln τ versus $1/T$ plot at 1500 Oe was extracted (Fig. S5). This curve was fitted using the formula $\tau^{-1} = CT^n + \tau_0^{-1}\exp(-U_{eff}/kT)$, which includes both Raman and Orbach processes, giving $n = 5.23$, $C = 0.00002$ s^{-1} K$^{-5.23}$, $U_{eff}/k = 319.6$ K and $\tau_0 = 1.3 \times 10^{-9}$ s. Similar to other zero-field SMMs,[51] applying a dc magnetic field (1500 Oe) to S-**1** could have partially or completely suppressed QTM, which increased its U_{eff}/k value (from 234.6 K to 319.6 K) and decreased its τ_0 value (from 4.1×10^{-8} s to 1.3×10^{-9} s).

Theoretical analysis of magnetic properties

Complete-active-space self-consistent field (CASSCF) analyses for two individual Dy^{III} fragments (Dy1 and Dy2) of S-**1**, based on its crystal structure, were performed using the OpenMolcas program[52] and the SINGLE_ANISO program (see the SI for details).[53–59] Table S2 lists the energy levels, $\boldsymbol{g}$ (g_x, g_y, g_z) tensors, and the predominant m_J values of the lowest eight Kramers doublets (KDs) for Dy1 and Dy2 of S-**1**, in which the predominant m_J values for the ground KDs are both equal to ±15/2, with $g_z \approx 20.000 > g_{x,y} \approx 0.000$, indicating that Dy1 and Dy2 have nearly perfectly axial anisotropies. Table S3 lists the m_J components for the lowest eight KDs in Dy1 and Dy2, in which the ground KDs of both Dy1 and Dy2 mostly consist of $m_J = \pm15/2$, and the first excited KDs of both Dy1 and Dy2 are mostly composed of $m_J = \pm13/2$. However, the higher excited KDs are all composed of several m_J states, which result in the formation of large transversal magnetic moments in the corresponding excited KDs for S-**1**.

The magnetization blocking barriers of Dy1 and Dy2 are shown in Fig. 7a and b, respectively. The transversal magnetic moments in the ground KDs of both Dy1 and Dy2 are close to $10^{-3}\mu_B$ ($1.2 \times 10^{-3}\mu_B$ for Dy1 and $1.4 \times 10^{-3}\mu_B$ for Dy2), leading to the quantum tunneling of magnetizations (QTMs) in their ground KDs, which are suppressed at low temperatures. The transversal magnetic moments in the first excited states of both Dy1 and Dy2 are close to $10^{-2}\mu_B$ ($3.6 \times 10^{-2}\mu_B$ for Dy1 and $5.5 \times 10^{-2}\mu_B$ for Dy2), leading to fast thermal-assisted QTMs (TA-QTMs) that are suppressed at low temperatures. However, for the second excited KDs, the fast TA-QTMs are allowed
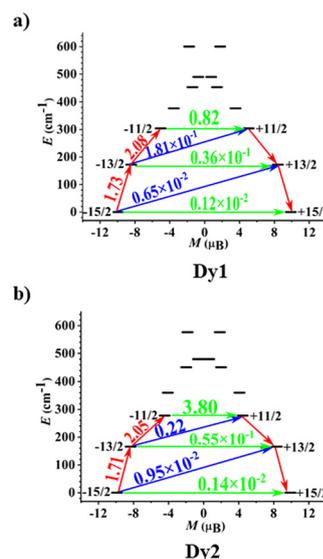
Fig. 7 Magnetization blocking barriers of individual Dy^{III} fragments [(a): Dy1; (b): Dy2] of S-**1**. The thick black lines represent the KDs as a function of their magnetic moment along the magnetic axis. The green lines correspond to diagonal quantum tunneling of magnetization (QTM) and the blue line represents off-diagonal relaxation process. The numbers at each arrow stand for the mean absolute value of the corresponding matrix element of the transition magnetic moment.

because of the larger transversal magnetic moments ($8.2 \times 10^{-1}\mu_B$ for Dy1 and $3.8\mu_B$ for Dy2). Therefore, the calculated energy barriers of Dy1 and Dy2 are 303.9 cm^{-1} and 277.6 cm^{-1}, respectively, which are larger than the experimental effective energy barrier (163.0 cm^{-1}, $H_{dc} = 0$ Oe). Even when QTM was suppressed by 1500 Oe, the experimental effective energy barrier (222.1 cm^{-1}, $H_{dc} = 1500$ Oe) remained lower than the calculated one. This suggests that in addition to QTM, there are Raman magnetic relaxation, anharmonic phonons, and other unfavourable effects in S-**1**.[56–59] Notably, the computed energy barriers of Dy1 and Dy2 of S-**1** (303.9 cm^{-1} and 277.6 cm^{-1}) were obviously larger than those of Zn$_2$Dy$_2$ SMMs with the same and similar L_{Schiff}^{2-} ligands ($\leq$229.1 cm^{-1}).[43–45]

Conclusions

In summary, (R)/(S)-2-methoxy-2-phenylacetic acids were successfully used to prepare a pair of Dy$_2$Zn$_2$ enantiomers, [Dy$_2$Zn$_2$(S-MPA)$_2$(L$_{Schiff}$)$_4$(DMF)$_2$]·2DMF (S-**1**) and [Dy$_2$Zn$_2$(R-MPA)$_2$(L$_{Schiff}$)$_4$(DMF)$_2$]·2DMF (R-**1**), based on the Schiff base ligand (E)-2-((2-hydroxy-3-methoxybenzylidene)amino)phenol. Their enantiomeric nature and chiral optical activities were confirmed from their CD spectra. S-**1** and R-**1** are rare, chiral Dy–Zn zero-field SMMs in that they exhibit a hysteresis loop at 3.0 K, and their U_{eff}/k value of 234.6 K is relatively large for Zn$_2$Dy$_2$ SMMs. In addition, their magnetic properties were explained by ab initio calculations. This work demonstrates that homochiral carboxylic acids, which are commonly used
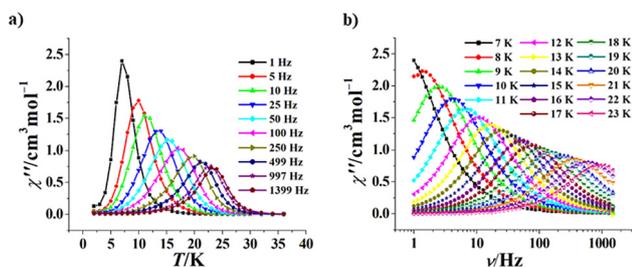
Fig. 6 χ'' versus T curves for S-**1** ($H_{dc} = 1500$ Oe) (a); and χ'' versus ν curves for S-**1** ($H_{dc} = 1500$ Oe) (b).

chiral ligands, can also be used to construct high-performing chiral 3d–4f Schiff base SMMs.

Conflicts of interest

There are no conflicts to declare.

Data availability

The data supporting this article have been included as part of the SI. Characterization data, computational details, X-ray crystallographic file in CIF format for *R*-**1** and *S*-**1**. See DOI: **https://doi.org/10.1039/d5dt01609f**.

CCDC 2463750 and 2463751 contain the supplementary crystallographic data for this paper.[60a,b]

References

1 J. Long, M. S. Ivanov, V. A. Khomchenko, E. Mamontova, J. M. Thibaud, J. Rouquette, M. Beaudhuin, D. Granier, R. A. S. Ferreira, L. D. Carlos, B. Donnadieu, M. S. C. Henriques, J. A. Paixao, Y. Guari and J. Larionova, *Science*, 2020, **367**, 671–676.

2 D.-P. Li, T.-W. Wang, C.-H. Li, D.-S. Liu, Y.-Z. Li and X.-Z. You, *Chem. Commun.*, 2010, **46**, 2929–2931.

3 X.-L. Li, C.-L. Chen, Y.-L. Gao, C.-M. Liu, X.-L. Feng, Y.-H. Gui and S.-M. Fang, *Chem. – Eur. J.*, 2012, **18**, 14632–14637.

4 X.-L. Li, M. Hu, Z. Yin, C. Zhu, C.-M. Liu, H.-P. Xiao and S. Fang, *Chem. Commun.*, 2017, **53**, 3998–4001.

5 H.-R. Wen, J.-J. Hu, K. Yang, J.-L. Zhang, S.-J. Liu, J.-S. Liao and C.-M. Liu, *Inorg. Chem.*, 2020, **59**, 2811–2824.

6 C.-M. Liu, D.-Q. Zhang, R.-G. Xiong, X. Hao and D.-B. Zhu, *Chem. Commun.*, 2018, **54**, 13379–13382.

7 X.-L. Li, A. Wang, M. Cui, C. Gao, X. Yu, B. Su, L. Zhou, C.-M. Liu, H.-P. Xiao and Y.-Q. Zhang, *Inorg. Chem.*, 2022, **61**, 9283–9294.

8 C.-M. Liu, R. Sun, B.-W. Wang, X. Hao and X.-L. Li, *Inorg. Chem.*, 2022, **61**, 18510–18523.

9 S.-D. Zhu, J.-J. Hu, L. Dong, H.-R. Wen, S.-J. Liu, Y.-B. Lu and C.-M. Liu, *J. Mater. Chem. C*, 2020, **8**, 16032–16041.

10 M. Atzori, K. Dhbaibi, H. Douib, M. Grasser, V. Dorcet, I. Breslavetz, K. Paillot, O. Cador, G. L. J. A. Rikken, B. Le Guennic, J. Crassous, F. Pointillart and C. Train, *J. Am. Chem. Soc.*, 2021, **143**, 2671–2675.

11 K. Dhbaibi, M. Grasser, H. Douib, V. Dorcet, O. Cador, N. Vanthuyne, F. Riobé, O. Maury, S. Guy, A. Bensalah-Ledoux, B. Baguenard, G. L. J. A. Rikken, C. Train, B. Le Guennic, M. Atzori, F. Pointillart and J. Crassous, *Angew. Chem., Int. Ed.*, 2023, **62**, e202215558.

12 B. E. Rez, J. Liu, V. Béreau, C. Duhayon, Y. Horino, T. Suzuki, L. Coolen and J.-P. Sutter, *Inorg. Chem. Front.*, 2020, **7**, 4527–4534.

13 C. A. Mattei, V. Montigaud, F. Gendron, S. Denis-Quanquin, V. Dorcet, N. Giraud, F. Riobé, G. Argouarch, O. Maury, B. Le Guennic, O. Cador, C. Lalli and F. Pointillart, *Inorg. Chem. Front.*, 2021, **8**, 947–962.

14 B. Lefeuvre, C. A. Mattei, J. F. Gonzalez, F. Gendron, V. Dorcet, F. Riobé, C. Lalli, B. Le Guennic, O. Cador, O. Maury, S. Guy, A. Bensalah-Ledoux, B. Baguenard and F. Pointillart, *Chem. – Eur. J.*, 2021, **27**, 7362–7366.

15 H. Huang, R. Sun, X.-F. Wu, Y. Liu, J.-Z. Zhan, B.-W. Wang and S. Gao, *Dalton Trans.*, 2023, **52**, 7646–7651.

16 R. Sessoli, D. Gatteschi, A. Caneschi and M. A. Novak, *Nature*, 1993, **365**, 141–143.

17 D. N. Woodruff, R. E. P. Winpenny and R. A. Layfield, *Chem. Rev.*, 2013, **113**, 5110–5148.

18 Y.-S. Meng, S.-D. Jiang, B.-W. Wang and S. Gao, *Acc. Chem. Res.*, 2016, **49**, 2381–2389.

19 C.-M. Liu, R.-G. Xiong, D.-Q. Zhang and D.-B. Zhu, *J. Am. Chem. Soc.*, 2010, **132**, 4044–4045.

20 P.-H. Guo, J.-L. Liu, J.-H. Jia, J. Wang, F.-S. Guo, Y.-C. Chen, W.-Q. Lin, J.-D. Leng, D.-H. Bao, X.-D. Zhang, J.-H. Luo and M.-L. Tong, *Chem. – Eur. J.*, 2013, **19**, 8769–8773.

21 L. Miao, M.-J. Liu, M. Zeng and H.-Z. Kou, *Inorg. Chem.*, 2023, **62**, 12814–12821.

22 C.-M. Liu, D.-Q. Zhang, X. Hao and D.-B. Zhu, *Inorg. Chem. Front.*, 2020, **7**, 3340–3351.

23 Z. Zhu, C. Zhao, T. Feng, X. Liu, X. Ying, X.-L. Li, Y.-Q. Zhang and J. Tang, *J. Am. Chem. Soc.*, 2021, **143**, 10077–10082.

24 Y.-Y. Zhu, C. Cui, Y.-Q. Zhang, J.-H. Jia, X. Guo, C. Gao, K. Qian, S.-D. Jiang, B.-W. Wang, Z.-M. Wang and S. Gao, *Chem. Sci.*, 2013, **4**, 1802–1806.

25 B.-F. Long, S. Yu, Z.-H. Zhu, Y.-L. Li, F.-P. Liang and H.-H. Zou, *Inorg. Chem. Front.*, 2022, **9**, 5950–5959.

26 X. Wang, M.-H. Du, H. Xu, L.-S. Long, X.-J. Kong and L.-S. Zheng, *Inorg. Chem.*, 2021, **60**, 5925–5930.

27 M.-X. Yao, Q. Zheng, F. Gao, Y.-Z. Li, Y. Song and J.-L. Zuo, *Dalton Trans.*, 2012, **41**, 13682–13690.

28 G. Li, X. Zhao, Q. Han, L. Wang and W. Liu, *Dalton Trans.*, 2020, **49**, 10120–10126.

29 D. Dermitzaki, A. Panagiotopoulou, M. Pissas, V. Psycharis and C. P. Raptopoulou, *ChemPlusChem*, 2024, **89**, e202400123.

30 C.-M. Liu, D.-Q. Zhang and D.-B. Zhu, *Inorg. Chem.*, 2013, **52**, 8933–8940.

31 C.-M. Liu, R. Sun, B.-W. Wang, F. Wu, X. Hao and Z. Shen, *Inorg. Chem.*, 2021, **60**, 12039–12048.

32 C.-M. Liu, R. Sun, X. Hao and B.-W. Wang, *Inorg. Chem.*, 2023, **62**, 20184–20193.

33 J.-S. Feng, M. Ren, Z.-S. Cai, K. Fan, S.-S. Bao and L.-M. Zheng, *Chem. Commun.*, 2016, **52**, 6877–6880.

34 C.-M. Liu, H.-H. Zou, Y.-Q. Zhang, X. Hao and X.-M. Ren, *Chin. J. Chem.*, 2025, **43**, 1051–1058.

35 Y. Chen, F. Ma, Y. Zhang, L. Zhao, K. Wang, D. Qi, H.-L. Sun and J. Jiang, *Inorg. Chem. Front.*, 2018, **5**, 2006–2012.

36 M. Feng, B.-H. Lyu, M.-H. Wang, W.-W. Wu, Y.-C. Chen, G.-Z. Huang, W.-Q. Lin, S.-G. Wu, J.-L. Liu and M.-L. Tong, *Inorg. Chem.*, 2019, **58**, 10694–10703.

37 Z. Zhu, C. Zhao, Q. Zhou, S. Liu, X.-L. Li, A. Mansikkamäki and J. Tang, *CCS Chem.*, 2022, **4**, 3762–3771.

38 C.-M. Liu, X. Hao and Y.-Q. Zhang, *Dalton Trans.*, 2025, **54**, 4159–4166.

39 B. Casanovas, S. Speed, M. S. El Fallah, R. Vicente, M. Font-Bardía, F. Zinna and L. Di Bari, *Dalton Trans.*, 2019, **48**, 2059–2067.

40 C.-M. Liu, D.-Q. Zhang, X. Hao and D.-B. Zhu, *Cryst. Growth Des.*, 2019, **19**, 4731–4737.

41 T. Han, J.-D. Leng, Y.-S. Ding, Y. Wang, Z. Zheng and Y.-Z. Zheng, *Dalton Trans.*, 2015, **44**, 13480–13484.

42 À. Tubau, F. Zinna, L. Di Bari, M. Font-Bardía and R. Vicente, *Dalton Trans.*, 2024, **53**, 13566–13582.

43 H. Ke, W. Wei, Y.-Q. Zhang, J. Zhang, G. Xie and S. Chen, *Dalton Trans.*, 2018, **47**, 16616–16626.

44 J. Li, R.-M. Wei, T.-C. Pu, F. Cao, L. Yang, Y. Han, Y.-Q. Zhang, J.-L. Zuo and Y. Song, *Inorg. Chem. Front.*, 2017, **4**, 114–122.

45 G.-P. Li, H.-F. Xie, S.-R. Yang, Y.-L. Fu, Y.-Q. Zhang and Y.-Y. Wang, *Chin. J. Chem.*, 2022, **40**, 2415–2420.

46 D. Casanova, M. Llunell, P. Alemany and S. Alvarez, *Chem. – Eur. J.*, 2005, **11**, 1479–1494.

47 Vipanchi, K. R. Vignesh, A. S. Armenis, D. I. Alexandropoulos and T. C. Stamatatos, *ChemPhysChem*, 2024, **25**, e202400385.

48 Y.-N. Guo, G.-F. Xu, P. Gamez, L. Zhao, S.-Y. Lin, R. Deng, J. Tang and H.-J. Zhang, *J. Am. Chem. Soc.*, 2010, **132**, 8538–8539.

49 C.-M. Liu, D.-Q. Zhang and D.-B. Zhu, *Dalton Trans.*, 2013, **42**, 14813–14818.

50 S. K. Langley, N. F. Chilton, B. Moubaraki and K. S. Murray, *Inorg. Chem.*, 2013, **52**, 7183–7192.

51 J. P. Costes, S. Titos-Padilla, I. Oyarzabal, T. Gupta, C. Duhayon, G. Rajaraman and E. Colacio, *Chem. – Eur. J.*, 2015, **21**, 15785–15796.

52 I. F. Galván, M. Vacher, A. Alavi, C. Angeli, F. Aquilante, J. Autschbach, J. J. Bao, S. I. Bokarev, N. A. Bogdanov, R. K. Carlson, L. F. Chibotaru, J. Creutzberg, N. Dattani, M. G. Delcey, S. S. Dong, A. Dreuw, L. Freitag, L. M. Frutos, L. Gagliardi, F. Gendron, A. Giussani, L. González, G. Grell, M. Y. Guo, C. E. Hoyer, M. Johansson, S. Keller, S. Knecht, G. Kovacevic, E. Källman, G. L. Manni, M. Lundberg, Y. J. Ma, S. Mai, J. P. Malhado, P. Å. Malmqvist, P. Marquetand, S. A. Mewes, J. Norell, M. Olivucci, M. Oppel, Q. M. Phung, K. Pierloot, F. Plasser, M. Reiher, A. M. Sand, I. Schapiro, P. Sharma, C. J. Stein, L. K. Sørensen, D. G. Truhlar, M. Ugandi, L. Ungur, A. Valentini, S. Vancoillie, V. Veryazov, O. Weser, T. A. Wesołowski, P.-O. Widmark, S. Wouters, A. Zech, J. P. Zobel and R. J. Lindh, *Chem. Theory Comput.*, 2019, **15**, 5925–5964.

53 L. F. Chibotaru, L. Ungur and A. Soncini, *Angew. Chem., Int. Ed.*, 2008, **47**, 4126–4129.

54 L. Ungur, W. Van den Heuvel and L. F. Chibotaru, *New J. Chem.*, 2009, **33**, 1224–1230.

55 L. F. Chibotaru, L. Ungur, C. Aronica, H. Elmoll, G. Pilet and D. Luneau, *J. Am. Chem. Soc.*, 2008, **130**, 12445–12455.

56 A. Lunghi, F. Totti, R. Sessoli and S. Sanvito, *Nat. Commun.*, 2017, **8**, 14620–14626.

57 F. Lu, W.-X. Guo and Y.-Q. Zhang, *Inorg. Chem.*, 2022, **61**, 295–301.

58 T. Shang, F. Lu, J. Tao and Y.-Q. Zhang, *J. Phys. Chem. A*, 2023, **127**, 3088–3095.

59 S. K. Langley, D. P. Wielechowski, V. Vieru, N. F. Chilton, B. Moubaraki, B. F. Abrahams, L. F. Chibotaru and K. S. Murray, *Angew. Chem., Int. Ed.*, 2013, **52**, 12014–12019.

60 (*a*) C.-M. Liu, X. Hao and Y.-Q. Zhang, CCDC 2463750 (*R*-**1**): Experimental Crystal Structure Determination, 2025, DOI: **10.5517/ccdc.csd.cc2npqtx**; (*b*) C.-M. Liu, X. Hao and Y.-Q. Zhang, CCDC 2463751 (*S*-**1**): Experimental Crystal Structure Determination, 2025, DOI: **10.5517/ccdc.csd.cc2npqvy**.